Synthesis and characterization of Th1−xLnxO2−x/2 mixed-oxides

5 AUTHORS, INCLUDING:

Denis Horlait
French National Centre for Scientific Resea…
38 PUBLICATIONS **196** CITATIONS

SEE PROFILE

Nicolas Clavier
French National Centre for Scientific Resea…
95 PUBLICATIONS **1,101** CITATIONS

SEE PROFILE

Nicolas Dacheux
French National Centre for Scientific Resea…
180 PUBLICATIONS **2,486** CITATIONS

SEE PROFILE

Renaud Podor
Institut de Chimie Séparative de Marcoule
151 PUBLICATIONS **1,409** CITATIONS

SEE PROFILE

Synthesis and characterization of $Th_{1-x}Ln_xO_{2-x/2}$ mixed-oxides

D. Horlait, N. Clavier, N. Dacheux *, R. Cavalier, R. Podor

ICSM - UMR5257 CNRS/CEA/UM2/ENCSM, Site de Marcoule, Bât. 426, BP 17171, 30207 Bagnols/Cèze, France

ABSTRACT

Several $Th_{1-x}Ln_xO_{2-x/2}$ mixed-oxides (Ln = Nd, Sm, Gd, Dy, Er or Yb) were prepared from oxalate precursors. Structural and microstructural investigations of both initial precursors and resulting oxides were undertaken by XRD, μ-Raman spectroscopy and SEM, with a particular attention paid to the $Th_{1-x}Nd_xO_{2-x/2}$ series.

For oxides, XRD and μ-Raman agreed well with the stabilization of the $Fm\bar{3}m$ structure up to x_{Nd} = 0.4, thanks to the concomitant creation of oxygen vacancies, as also confirmed by μ-Raman. Then, a structural transition to the $Ia\bar{3}$ superstructure occurred. For $x_{Nd} \geq 0.49$, mixed-oxides with an additional hexagonal Nd_2O_3 phase were prepared.

Besides, the unit cell parameter of the $Th_{1-x}Ln_xO_{2-x/2}$ series followed a quadratic relation versus the x substitution rate as a result of the combination between modifications of cationic radius and cation coordination, and the decrease of O–O repulsion linked to the presence of oxygen vacancies.

© 2012 Elsevier Ltd. All rights reserved.

1. Introduction

REE-doped thoria (REE = rare-earth element) is of great interest in view of its promising applications in various areas of energy technology such as oxygen sensors [1–4] or as potential nuclear fuel in several future concepts [5–12]. Indeed, due to the promising resources of thorium ores and to the possibility to achieve a nuclear fuel cycle which considerably reduces the amount of long-live radioactive wastes, a renewal of interest of thoria-based nuclear fuel cycles recently emerged. As an example, the possibility to reduce the radiotoxicity of waste in the current nuclear fuel cycle by incorporating the minor actinides in new UO_2- or ThO_2-based fuels then performing their transmutation in fast neutron reactors is currently examined [11–13]. Likewise, ThO_2–Er_2O_3–PuO_2 or ThO_2–Gd_2O_3–PuO_2 ternary systems were recently envisaged as new fuel elements [6,7].

In all foreseen Th-based fuel cycles, the lanthanide elements would be an important part of the fission products. Likewise, americium and curium, for whose neodymium is often employed as a surrogate [14] would be quantitatively produced by successive neutron captures. In this context, since Am [14–17], Cm [14] and the major part of the lanthanide elements are generally stable at the trivalent oxidation state in solids, the formation of $Th^{IV}_{1-x}Ln^{III}_xO_{2-x/2}$ mixed-oxide series needed to be assessed in order to anticipate then optimize properly the life-cycle of such potential fuels.

Over the past 50 years, only a few studies were dedicated to the $Th_{1-x}Ln_xO_{2-x/2}$ mixed-oxides [18–24]. All of them confirmed that ThO_2 crystallizes in the same structure than CeO_2, PuO_2 and UO_2 (fluorite, $Fm\bar{3}m$ space group, commonly called F-type structure). This crystal structure was stabilized during the incorporation of trivalent elements up to about 50 at.% of the cations for La or Nd [20,21] and to less than 10 at.% of Yb or Lu [18,19]. The incorporation of trivalent elements was examined thanks to the use of fluorite-type $Hf_{1-x}Ln_xO_{2-x/2}$ [25,26], $Zr_{1-x}Gd_xO_{2-x/2}$ [27–29], or $Ce_{1-x}Ln_xO_{2-x/2}$ [30–40] solid solutions analogues with the help of several techniques (molecular dynamics [29,32], life-time positon spectroscopy [33], EXAFS [34] or μ-Raman spectroscopy [35–40]). All these techniques suggested the existence of a mechanism involving the concomitant creation of oxygen vacancies ($V_{\ddot{O}}$) to counterbalance the lack of positive charges due to the incorporation of the trivalent lanthanide.

To our knowledge, this mechanism of incorporation was never clearly evidenced for thoria-based solid solutions. In this aim, experiments combining XRD and μ-Raman spectroscopy were carried out on $Th_{1-x}Ln_xO_{2-x/2}$ samples to check the presence of oxygen vacancies.

Various samples were examined in this work: the $Th_{1-x}Nd_xO_{2-x/2}$ series ($0 \leq x_{Nd} \leq 1$) was selected to precisely assess the relation between the REE incorporation rate (x) and the crystalline structure adopted while $Th_{0.90}Ln_{0.10}O_{1.95}$ and $Th_{0.70}Ln_{0.30}O_{1.85}$ samples (with Ln = Sm, Gd, Dy, Er or Yb) were considered to study the influence of the ionic radius of the rare earth ion (REE) with a constant stoichiometry. All the mixed-oxides were prepared from oxalate precipitates: the quantitative and homogeneous precipitation of thorium and lanthanide

* Corresponding author. Tel.: +33 466339205.
E-mail address: nicolas.dacheux@univ-montp2.fr (N. Dacheux).

elements with oxalic acid was chosen to prepare the starting precursors of expected solid solutions since their use usually led to an improvement of the final sample homogeneity [41–46] and to the optimization of some properties of interest, such as sintering capability or chemical durability [45–53].

The relationships between the structure and the microstructure of the starting oxalate precursors and that of the resulting mixed-oxides was particularly followed. Then, couplings between XRD and μ-Raman spectroscopy characterizations allowed following the trivalent element incorporation in the thoria structure as well as the associated structural modifications. Finally, the variation of the unit cell parameters versus the Ln^{III} substitution ratio was followed all along the $Th_{1-x}Ln_xO_{2-x/2}$ series.

2. Experimental

2.1. Synthesis

$ThNO_3 \cdot 5H_2O$ and $LnCl_3 \cdot nH_2O$ or $LnNO_3 \cdot nH_2O$ (Aldrich, ≥99.9% chemical purity) were used as starting reagents. They were dissolved in 0.5 M HNO_3 solution in order to obtain final cations concentrations of about 1 M. The mixture was then poured drop wise into a large excess of oxalic acid (Merck, ≥99% purity) at room temperature under stirring. The precipitates rapidly formed were aged for few minutes, then filtered, washed several times with deionized water and finally dried at 90 °C. The characterization of the as-obtained mixed-oxalates was mainly driven by the means of XRD, IR and μ-Raman spectroscopies as detailed in Section 3.1.

For all the samples, both thorium and lanthanide elementary concentrations were determined in the supernatant by the means of ICP-AES analyses (performed on a Spectro Arcos EOP). Whatever the sample considered, less than 1% of both elements remained in the solution, confirming the quantitative precipitation of lanthanide and thorium, as expected from the low solubilities reported in literature for thorium and REE oxalates [54,55].

Oxalate samples were fully converted to resulting oxides through a thermal treatment at 1000 °C in air for 1 h in alumina boats.

The precise chemical composition of the resulting oxides determined from EDS data (Table 1) were compared to that expected. The good agreement between expected and experimental x ratios clearly confirmed that both thorium and trivalent lanthanide elements were quantitatively precipitated as oxalate precursors. Moreover, for single phase mixed-oxides, successive X-EDS analyses always showed weak dispersion of the results indicating a homogeneous cations distribution within the samples.

2.2. XRD measurements

X-ray powder diffraction (XRD) patterns were collected with a step of 0.01° (2θ) and a counting time of 1.5 s step^{-1}, using a Bruker D8 Advance X-ray diffractometer (Cu $K\alpha_{1,2}$ radiation, λ = 1.5418 Å) equipped with a linear Lynx-eye detector. XRD pattern of corundum (NIST standard reference material 676a) was used as reference to estimate the resolution of the apparatus. The mixed-oxides lattice parameters were refined from powder diffraction profiles using a profile matching procedure (Le Bail method) implemented in the Fullprof suite software [56].

2.3. TG/DT analysis

The thermal conversion of the starting oxalates to the final mixed-oxides was followed using a Setaram Setsys Evolution TGA/DTA (thermo-gravimetric/differential thermal analyzer). The furnace was always operating under dry air atmosphere from room temperature to 1000 °C with a heating rate of 5 °C min^{-1}.

2.4. IR

Infra-Red spectra of the mixed-oxalates were undertaken using a Perkin-Elmer Spectrum IR-FT 100 device, working with an ATR (Attenuated Total Reflectance) assembly. All the spectra were collected in the 380–4000 cm^{-1} range, considering the average of 4 scans with a resolution of 4 cm^{-1}.

Table 1
Experimental (X-EDS) and expected chemical compositions with corresponding unit cell parameter (a).

Loading element	Expected x ($Th_{1-x}Ln_xO_{2-x/2}$)	Experimental x (X-EDS)	Phase type	F- or C- unit cell parameters (Å)[a]
ThO_2	0	0	F	5.5926 (2)
Nd	0.05	0.05	F	5.5982 (2)
	0.10	0.10	F	5.6008 (1)
	0.12	0.12	F	5.6025 (2)
	0.15	0.16	F	5.6035 (2)
	0.25	0.25	F	5.6061 (2)
	0.30	0.29	F	5.6085 (1)
	0.35	0.34	F[b]	5.6075 (2)
	0.45	0.42	F[b]	5.6067 (4)
	0.45	0.45	C + F[c]	5.6056 (4)
	0.50	0.49	C + A	5.6042 (3)
	0.60	0.60	C + A	5.6060 (3)
	0.80	0.84	C + A	–
	0.95	0.97	C + A	–
	1	1	A	–
Sm	0.10	0.11	F	5.5958 (2)
	0.30	0.33	F	5.5934 (2)
Gd	0.10	0.11	F	5.5890 (2)
	0.30	0.27	F	5.5787 (2)
Dy	0.10	0.09	F	5.5892 (2)
	0.30	0.28	F	5.5731 (2)
Er	0.10	0.10	F	5.5863 (2)
	0.30	0.30	F + C	–
Yb	0.10	0.13	F	5.5787 (2)
	0.30	0.29	F	5.5495 (3)

[a] For comparison purpose, a and $a/2$ were reported for F- and C-type structures, respectively. Standard uncertainties are given with refinement results by Fullprof.
[b] C-type nanometric domains also evidenced by μ-Raman.
[c] C-type superstructure lines hardly detectable on XRD patterns (Fig. 4), probably indicating a mixture of C- and F-type phases.

2.5. μ-Raman

μ-Raman spectra were collected with the help of a Horiba-Jobin Yvon Aramis apparatus equipped with He–Ne ($\lambda = 632.8$ nm, 13 mW) laser and an edge filter. The laser beam was focused on the sample using an Olympus BX 41 microscope, resulting in a spot area of about 1 μm². At least three different locations were investigated at the surface of each sample, usually considering a dwell time of 3 s and an average of 10 scans.

2.6. SEM

SEM observations were performed with a FEI Quanta 200 environmental scanning electron microscope (ESEM) using a field-emission gun. Optimal imaging conditions were determined for each compound, leading to the use of different detectors (LFD, large-field detector under low vacuum or BSED, back-scattering electron detector under high vacuum) and various settings of acceleration voltage (typically between 2 and 15 kV) and working distance (5–9 mm). Some oxalate calcinations were followed in situ thanks to a furnace implemented directly in the microscope chamber, using operating settings already described by Podor et al. for CeO_2 [57–59].

2.7. EDS

The precise lanthanide incorporation rates, x, in the $Th_{1-x}Ln_xO_{2-x/2}$ series were determined from energy dispersive spectrometry (EDS) analyses coupled with the SEM device using a Bruker AXS X-Flash 5010 detector. Each powdered mixed-oxide was embedded in an epoxy resin, polished to the 1 μm grid and carbon coated prior making such analyses. EDS results were then obtained from at least twelve different analyses (twenty for polyphased samples). At least 400,000 counts spectra were collected by the EDS detector using routinely an optimal working distance of 11.4 mm and an acceleration voltage of 15 kV. Assuming all the errors associated to such experiments, the uncertainties correlated to the average x values determined for each compound were assumed to ±0.01.

3. Results and discussion

3.1. Structural characterization of the oxalates precursors

IR and μ-Raman spectroscopy were both used as a way to assess the preparation of oxalates precursors. A few spectra of thorium-neodymium based compounds are presented in supplementary data. From this data, one can find all the C–C and C–O related vibration bands of oxalate-based metal organic frameworks. The positions and assignment of all the observed bands are also given in supplementary data according to that proposed by Clavier et al. [42] and Morris and Hobart [60]. From IR and μ-Raman, the progressive splitting of some bands was noted when increasing the lanthanide content which suggests structural modifications with x.

Such structural modifications were also evidenced by XRD characterization. Selected XRD patterns of Th/Nd and of Th/Ln mixed-oxalates are presented in Fig. 1a and b, respectively. The structure of such mixed-oxalates was found to be dependent on the nature and the amount of the incorporated trivalent lanthanide element.

Thorium oxalate pattern was found to be consistent with that reported for $Th(C_2O_4)_2 \cdot 2H_2O$ in its $C2/c$ monoclinic form [42]. This structure was maintained up to $x_{Nd} = 0.16$. For $0.21 \leq x_{Nd} \leq 0.84$, the prepared oxalates were always polyphased. XRD revealed the presence of two to three crystalline structures in this range of composition: monoclinic $C2/c$ typical of $Th(C_2O_4)_2 \cdot 2H_2O$,
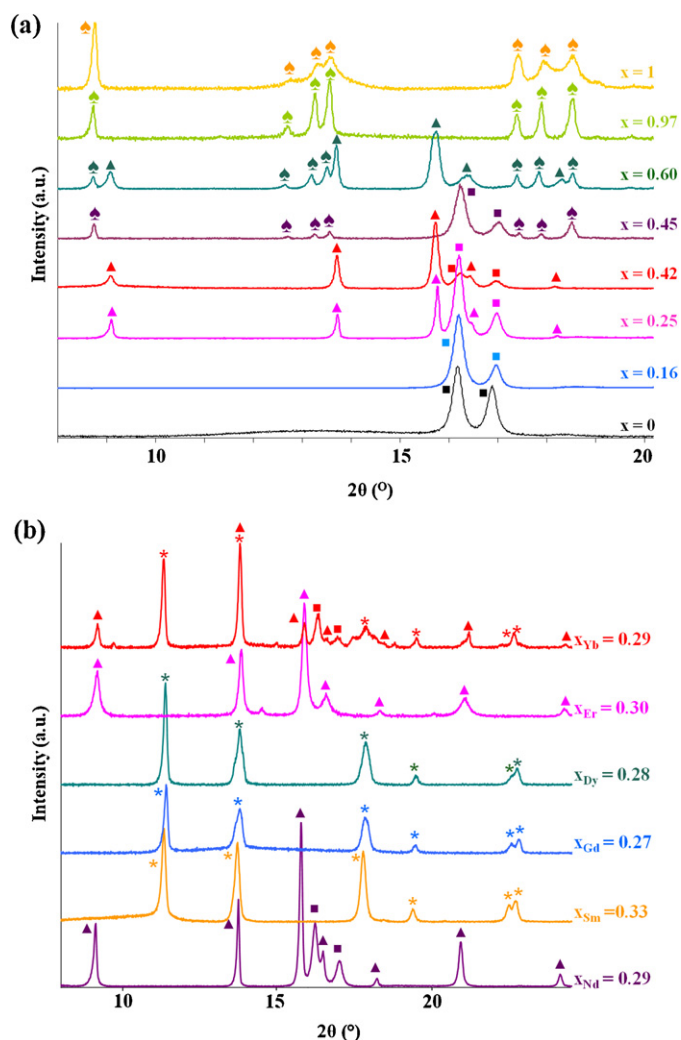
Fig. 1. XRD patterns of Th/Nd (a) and of Th/Ln ($x \approx 0.3$) (b) mixed-oxalate precursors. Following symbols were use to point out the characteristic XRD lines of the different structures. (▲) Hexagonal $P6_3/mmc$; (♠) monoclinic $P2_1/c$; (■) monoclinic $C2/c$; (*) monoclinic $C2/m$.

hexagonal $P6_3/mmc$ [43] and monoclinic $P2_1/c$, which corresponds to the most common structure of $Nd(C_2O_4)_{1.5} \cdot 5H_2O$ [60–62]. Finally, for $x_{Nd} = 0.97$ and $x_{Nd} = 1$, the monoclinic $P2_1/c$ structure was the only one stabilized.

The XRD diagrams of Th/Ln mixed-oxalates ($x \approx 0.3$, Ln = Nd, Sm, Gd, Dy, Er or Yb, Fig. 1b) showed that the nature of the stabilized structure of thorium–lanthanide mixed-oxalates was highly dependent on the nature and the ionic radius of the trivalent element incorporated. Indeed, Nd-based oxalates were always polyphased, while single phase monoclinic $C2/m$ structure was stabilized for Sm, Gd and Dy (which was previously reported for various oxalates such as $Th(C_2O_4)_2 \cdot 6H_2O$ [63–66], $U(C_2O_4)_2 \cdot 6H_2O$ [67] or $Y(C_2O_4)_{1.5} \cdot 2H_2O$ [68]). Finally, the single phase Er-based oxalate samples crystallized with the hexagonal $P6_3/mmc$ structure while Yb-loaded oxalate was constituted by the three aforementioned structures ($P6_3/mmc$, $C2/m$ and $C2/c$ space groups).

3.2. Conversion of precursors to mixed-oxides

The conversion of the oxalates into mixed-oxides was performed through a thermal treatment in air at 1000 °C. The conversion of several Th/Nd oxalate samples ($x = 0, 0.10, 0.29, 0.60$,

0.84 and 1) was followed by TGA/DTA. All these experiments revealed two successive weight losses associated to the release of constitutive water molecules (above 120 °C and up to 320 °C), leading to the formation of anhydrous oxalates. These latter were further decomposed above $T \approx 350$ °C to finally form the resulting mixed-oxides. It is worth noting that this oxalate decomposition always occurred in one step even for the polyphased samples for which the temperature distinction for all phases remained very difficult. This was likely due to the close temperatures of oxalates decomposition of $Th(C_2O_4)_2$ and $Nd(C_2O_4)_{1.5}$ (respectively located
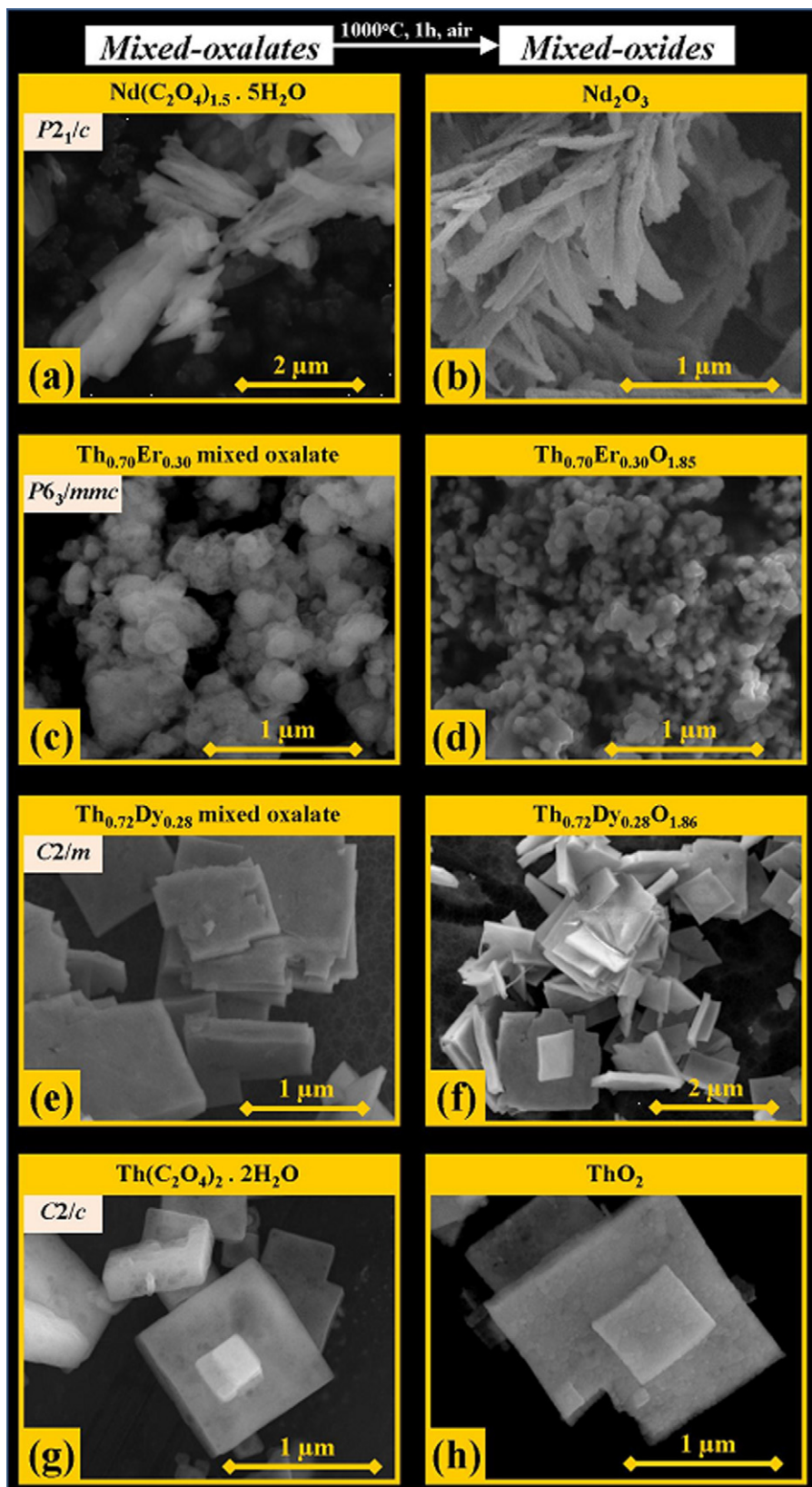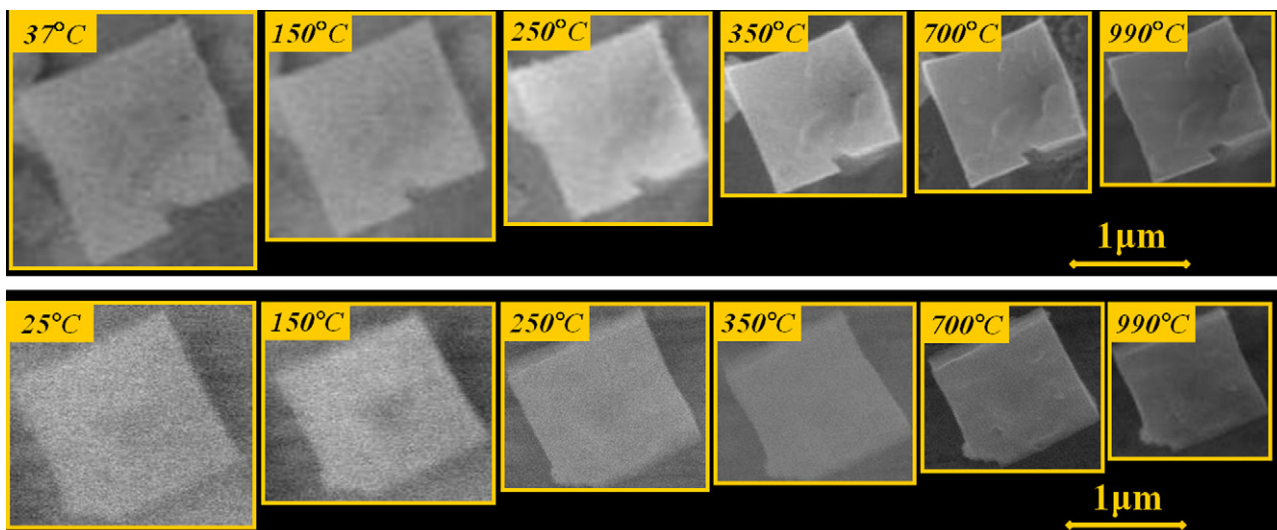

Fig. 2. SEM micrographs of Th/Nd mixed-oxalates and resulting mixed-oxides.

Fig. 3. In situ observation of the conversion of Th/Nd and Th/Dy oxalate precursors to the final $Th_{0.90}Nd_{0.10}O_{1.95}$ (up row) and to $Th_{0.72}Dy_{0.28}O_{1.86}$ (bottom row) solid solutions monitored by HT-ESEM. The magnification and the grain initially selected were conserved for both samples.

at 385 °C and 415 °C from DTA experiments, in agreement with the data reported in literature [69–72]. Finally, no additional weight loss was observed above 550 °C [52]. The thermal treatment of all the oxalate precursors at 1000 °C appeared thus suitable to ensure the completion of the conversion.

3.3. Microstructures

The microstructures of all oxalate and oxide samples were observed by SEM (Fig. 2). In addition, for some of the single phase precursors, the thermal conversion from oxalate to oxide was also followed through in situ ESEM experiments (Fig. 3). From the comparison of SEM observations and XRD results (Fig. 2 and Fig. 1, respectively), the nature of the crystalline structure adopted by a mixed–oxalate clearly impacted the resulting final microstructure. Indeed, compounds crystallizing with the monoclinic $P2_1/c$ were associated to slat shape (Fig. 2a) [35], while samples presenting the $P6_3/mmc$ space group exhibited spherical shape (Fig. 2c). Both monoclinic $C2/m$ and $C2/c$ type compounds appeared as thin square plates (Fig. 2e and g, respectively) [73]. The microstructure of all the samples was always kept during the conversion of

starting oxalates to final oxides (Figs. 2 and 3) despite the considerable successive weight losses (about 50% of the initial mass) and volume reduction (about 65% of the initial volume) observed. The powder microstructure of resulting oxides was thus clearly dependent on the microstructure and thus linked to the initial crystal structure of the oxalate precursor.

For ThO_2 to $Th_{0.58}Nd_{0.42}O_{1.79}$, micrometric square plates shapes were inherited from the oxalate microstructure (Fig. 2h). For $x_{Nd} \geq 0.21$, several microstructures were observed and associated to the polyphased systems of the starting oxalate precursors. Finally, for $Th_{0.03}Nd_{0.97}O_{1.515}$ and Nd_2O_3 (Fig. 2b), only grains with a slat shape (few micrometers in length) were observed.

3.4. XRD characterization of the resulting mixed-oxides

Selected XRD patterns of $Th_{1-x}Nd_xO_{2-x/2}$ mixed-oxides obtained after firing the initial precursors at 1000 °C are gathered in Fig. 4. XRD diagram of pure ThO_2 only showed the characteristic features of the $Fm\bar{3}m$ fluorite structure (F-type) that appeared in good agreement with literature [18–24]. This structure was stabilized up to $x_{Nd} \leq 0.42$. As detailed elsewhere [32–35,74–76], the
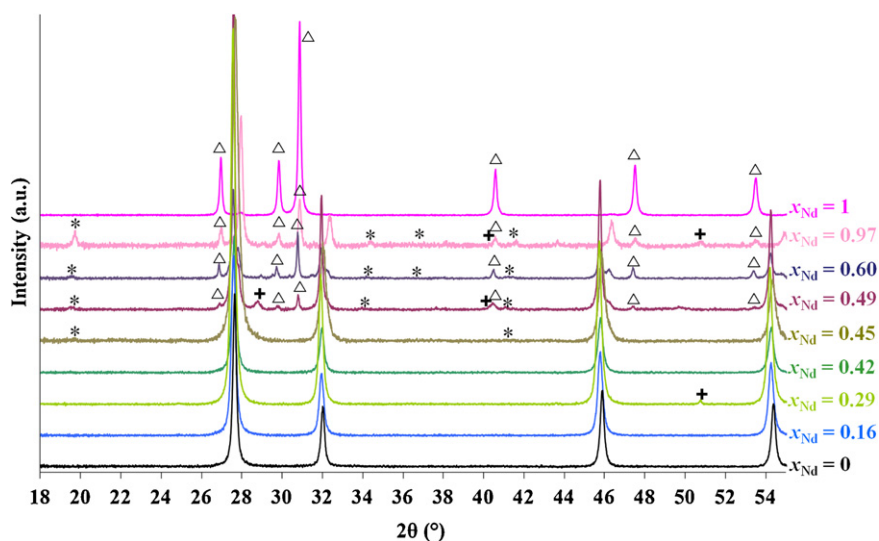
Fig. 4. XRD patterns obtained for the $Th_{1-x}Nd_xO_{2-x/2}$ series. XRD characteristic lines of the C-type structure are pointed out by stars (*), while that of A-type (Nd_2O_3) are denoted by triangles ($\triangle$). The crosses (+) are related to the sample holder.

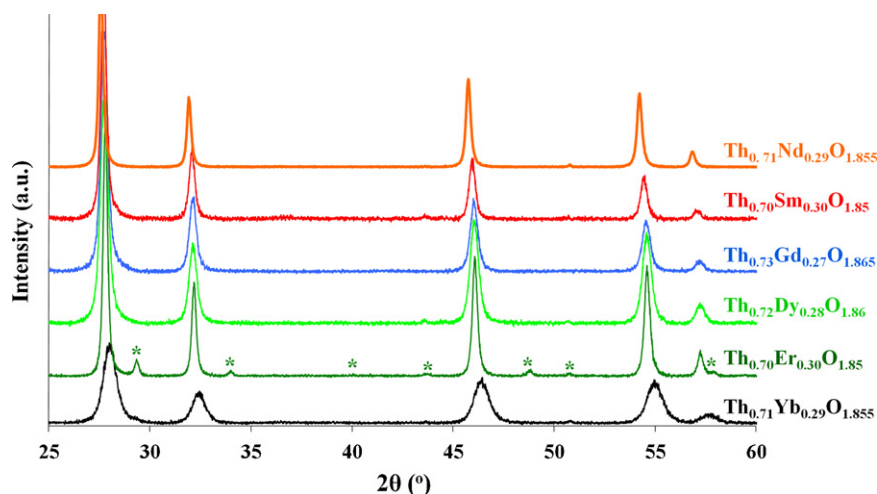**Fig. 5.** XRD patterns obtained for the $Th_{0.7}Ln_{0.3}O_{1.85}$ series (Ln = Nd, Sm, Gd, Dy, Er or Yb). Characteristic lines of C-type $Th_{0.70}Er_{0.30}O_{1.85}$ are pointed out by stars (*).

stabilization of the fluorite crystal symmetry despite the incorporation of an aliovalent cation was presumably made possible thanks to the concomitant creation of randomly distributed oxygen vacancies. Weak additional XRD lines located at about 20° and 42° (as pointed out by stars in Fig. 4) associated to the strongest characteristic lines of the cubic $Ia\bar{3}$ superstructure (C-type structure) [77–79] were noted for $x_{Nd} = 0.45$ while all the XRD lines characteristic of this structure were above this chemical composition (Fig. 4). This kind of structural transition from $Fm\bar{3}m$ to $Ia\bar{3}$ space group was widely reported for $Ce_{1−x}Ln_xO_{2−x/2}$ solid solutions [35,80–84,34,85,86], but, to our knowledge, the formation of a C-type $Th_{1−x}Ln_xO_{2−x/2}$ single phase sample was never reported up to now. The field of existence of single-phase C-type compounds appeared to be very narrow. Indeed, polyphased systems, composed of additional hexagonal $P\bar{3}1m$ structure (A-type, typical of Nd_2O_3) were prepared for $x_{Nd} \geq 0.49$, which appeared in good agreement with the limit of incorporation reported by Mathews et al. [22]. A + C polyphased oxides were then obtained even for the lowest thorium content (i.e. $Th_{0.03}Nd_{0.97}O_{1.515}$), confirming the very low "solubility" of thorium [18,22,24] and more generally of tetravalent cations [34,84,87,81] within the A-type structure characteristic of lanthanide sesquioxides from lanthanum to neodymium. Besides, the refined unit cell parameter a of $Th_{0.51}Nd_{0.49}O_{1.755}$ and $Th_{0.40}Nd_{0.60}O_{1.70}$ were very close to that of $Th_{0.55}Nd_{0.45}O_{1.775}$, indicating that the compositions of the C and the A phases of polyphased $Th_{1−x}Nd_xO_{2−x/2}$ were respectively close to "$Th_{0.55}Nd_{0.45}O_{1.775}$" and to "$Nd_2O_3$". Finally, as it was expected, only the A-type diffraction lines were denoted on the XRD pattern of Nd_2O_3 (see JCPDS file # 00-043-1023).

F-type features were always solely observed on the XRD patterns of $Th_{0.90}Ln_{0.10}O_{1.95}$ and $Th_{0.70}Ln_{0.30}O_{1.85}$ solid solutions (Ln = Nd, Sm, Gd, Dy, Er or Yb, Fig. 5) except for $Th_{0.70}Er_{0.30}O_{1.85}$ for which two crystalline phases (F- and C-type structures) were evidenced. Likewise, it should be pointed out that for $Th_{0.71}Yb_{0.29}O_{1.855}$, the XRD lines were broad, yet almost perfectly symmetrical, which indicated a low level of crystallization. Such difficulty to obtain well-crystallized single phase mixed-oxides with heavy trivalent lanthanide element was presumably due to steric effect. Indeed, Th and heavy REE ionic radii ($^{(8)}$Th^{IV} ionic radius is 1.05 Å, and heavy $^{(8)}$Ln^{III} ionic radii range from 1.004 Å for Er to 0.977 Å for Lu) are too different to allow the stabilization of the cubic solid solutions [18–22]. As a consequence, the solubility limit of trivalent lanthanide in thoria available from literature data [18–22] appears to gradually decrease from lanthanum ($x_{La} = 0.50$) [18–21] to lutetium ($x_{Lu} \leq 0.10$) [19]. However, some of the

mixed-oxides prepared from oxalate route, such as $Th_{0.72}Dy_{0.28}O_{1.86}$ were found to be homogeneous and single phase although they contain much more trivalent lanthanide element than usually admitted to prepare single phase samples [18–22]. This latter point underline the interest of using oxalate route to prepare final thorium-lanthanide oxides with a significant extend of the incorporation capacity of REE in thoria as it was already evidenced for ceria based samples [34,35].

3.5. Unit cell parameter variation

The unit cell parameter a of all F-type and C-type solid solutions, obtained by refinement of XRD patterns, are gathered in Table 1 and Fig. 6. For $Th_{1−x}Nd_xO_{2−x/2}$ series, as the C-type unit cell could be built from eight original fluorite cells (see unit cells representations in [35]), F- and C-type unit cell parameter could be directly compared by considering $a/2$ value for C-type cells [35,77,78]. The value obtained for ThO_2 ($a = 5.593 \pm 0.003$ Å) appears in good agreement with that reported in literature [19–22,88–90]. Likewise, the a values of $Th_{1−x}Ln_xO_{2−x/2}$ solid solutions agree well with the few available data [19,21,22].

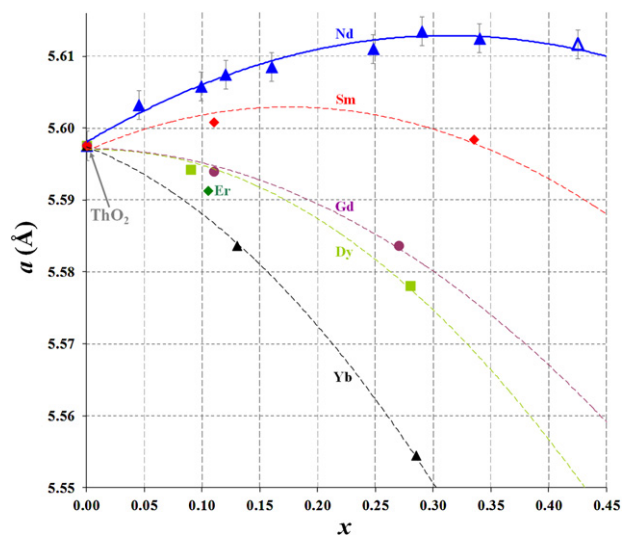**Fig. 6.** Variation of $Th_{1−x}Ln_xO_{2−x/2}$ fluorite unit cell parameter versus x substitution rate. For C-type $Th_{0.58}Nd_{0.42}O_{1.79}$ ($\triangle$), $a/2$ was considered for comparison purposes.

Two opposite phenomena can explain the variation of the unit cell parameter with the incorporation of a trivalent lanthanide element in the ThO_2 structure. On the one hand, the incorporation of a larger (from La to Gd) or of a smaller cation (from Dy to Yb) than Th^{4+} induces the expansion or shrinkage of the unit cell, respectively [91]. Thus, for the same incorporation rate, the heavier the trivalent lanthanide element, the lower the unit cell parameter (Fig. 6) [91]. On the other hand, the concomitant creation of oxygen vacancies and the progressive decrease of metal coordination number from 8 to 6 led to the contraction of the unit cell. As a consequence, even if the ionic radii of Gd^{3+} and Th^{4+} are very close in the eightfold coordination (1.053 Å and 1.050 Å, respectively [91]), the unit cell parameter of $Th_{1-x}Gd_xO_{2-x/2}$ series was found to decrease. Conversely, the increase of a as a function of x was only observed for $Th_{1-x}Nd_xO_{2-x/2}$ solid solutions (Fig. 6).

Moreover, the variation of the unit cell parameter as a function of the substitution rate (x) obviously followed a polynomial variation for $Th_{1-x}Nd_xO_{2-x/2}$ samples, as it was reported for $Ce_{1-x}Nd_xO_{2-x/2}$ [35] or for $Th_{1-x}Sm_xO_{2-x/2}$ and $Th_{1-x}Eu_xO_{2-x/2}$ series [19]. This non-linear variation was also confirmed for the other $Th_{1-x}Ln_xO_{2-x/2}$ series [35]. Moreover, for $Th_{1-x}Nd_xO_{2-x/2}$, a continuous variation of the unit cell parameter was observed in spite of the structural transition from F- to C-type. This was likely due to the great similarities between both structures, since C-type structure results in the ordering of the oxygen vacancies in the F-type one.

Similarly to what was widely reported for cubic $Ce_{1-x}Ln_xO_{2-x/2}$ solid solutions, the non-linear variation of a versus the trivalent REE incorporation rate x was fitted according to the following quadratic function [30,92,93,99]:

$$a(\text{Å}) = Ax^2 + Bx + C$$

where A, B and C correspond to three parameters obtained from the fitting of experimental results.

For the $Th_{1-x}Nd_xO_{2-x/2}$ series, the unit cell parameters a (expressed in Å) calculated by polynomial regression were $A = -0.1515$ Å, $B = 0.094$ Å and $C = 5.593$ Å. Such non-linear variation was already explained for analogous $Ce_{1-x}Ln_xO_{2-x/2}$ solid solutions [74–76,87]. Indeed, shrinkage of the Ce–O and Ln–O bond lengths with increasing x was evidenced. Such phenomenon was the direct consequence of the decrease of oxygen/oxygen repulsions in the structure when increasing the concentration of oxygen vacancies. However, since this effect was not directly proportional to x, a non-linear contraction of the unit cell was observed. Nevertheless, even if the vegardian variation [94,95] was not achieved, this continuous variation remains consistent with the formation of single-phase solid solutions [35] as it was also evidenced for other mixed systems, such as $(Ga_{1-x}Zn_x)(N_{1-x}O_x)$ [96] or $Ba_xSr_{1-x}SO_4$ [97].

3.6. μ-Raman characterization of the mixed-oxides

Simultaneously to the XRD characterization, further exploration of $Th_{1-x}Ln_xO_{2-x/2}$ samples was carried out by μ-Raman spectroscopy. The μ-Raman spectra of $Th_{0.90}Ln_{0.10}O_{1.95}$ and $Th_{0.70}Ln_{0.30}O_{1.85}$ solid solutions were all similar to that of $Th_{0.90}Nd_{0.10}O_{1.95}$ and $Th_{0.71}Nd_{0.29}O_{1.855}$, respectively. Only the spectra obtained for $Th_{1-x}Nd_xO_{2-x/2}$ solid solutions are then presented and discussed in Fig. 7.

As expected from the previous μ-Raman characterizations of ThO_2 [98] or $Ce_{1-x}Ln_xO_{2-x/2}$ solid solutions [35–39,74,75,99], the presence of the F_{2g} vibration mode was observed at about 460 cm^{-1} in the spectra of the $Th_{1-x}Nd_xO_{2-x/2}$ series (except for Nd_2O_3). This mode corresponds to the vibration of the M–O bond when the cation is surrounded in F- or C-type structure by eight oxygen atoms. As a consequence, this mode was the only observed for ThO_2 [98]. In order to quantitatively compare the variations in intensities of the other μ-Raman bands observed, the intensity of the F_{2g} mode band was used as a reference. In this aim, all the
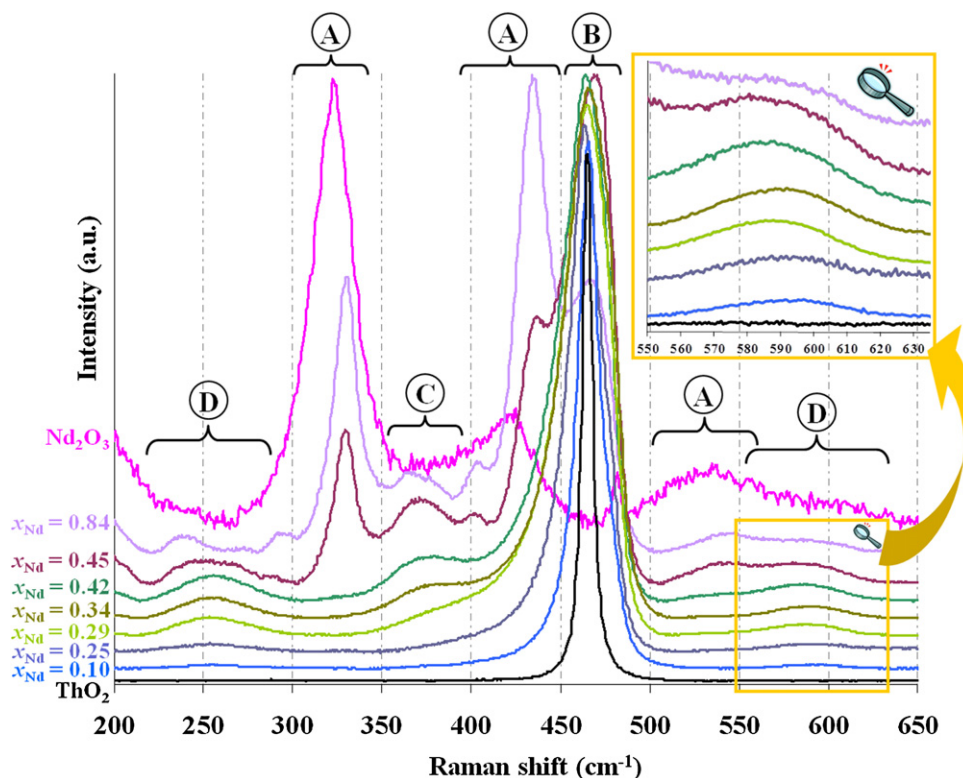
Fig. 7. μ-Raman spectra of $Th_{1-x}Nd_xO_{2-x/2}$ samples. Assignment of the vibration modes related to A-type structure (A) [104]; F_{2g} fluorite (B); C-type structure (C) and to M–O bonds in F- and C-type structure with the cation M surrounded by one or several oxygen vacancies (D).

spectra presented in Fig. 7 were normalized to get the same maximum height for the F_{2g} mode (excepted for Nd_2O_3 for which this mode does not appear).

The apparition of a new broad band centered at about 595 cm^{-1} was noted when incorporating trivalent element in the structure, even for the lower neodymium contents (insert in Fig. 7). For $Ce_{1-x}Ln_xO_{2-x/2}$ analogues, this "two-component" band was widely reported and was ascribed to the A_{1g} and F_{2g} vibration modes of the M–O bond with the presence of oxygen vacancies in the close vicinity of M [35–39,74,75,99]. Simultaneously, a second band appeared at about 260 cm^{-1}. This latter was less reported but was assigned to the same A_{1g} vibration mode [35,38]. When increasing the x_{Nd} value, the relative intensities of both bands were found to increase then finally reached their maxima for $x_{Nd} = 0.42$ and $x_{Nd} = 0.45$, i.e. for the compositions which are expected to contain the higher amounts of oxygen vacancies. All these results thus indicated that the stabilization of trivalent lanthanide in thoria-based solid solutions was made possible thanks to the concomitant creation of oxygen vacancies [35,99].

From the study of analogous C-type $Ce_{1-x}Ln_xO_{2-x/2}$ samples [35,99,100], one can also expect the presence of a band located near to 370 cm^{-1} in the $Th_{1-x}Ln_xO_{2-x/2}$ spectra, only characteristic of the modification occurring during the F to C-type structure transition (oxygen vacancies ordering and creation of a second cationic crystallographic site). Although this band was observed for all the samples presenting a C-type phase from XRD results, it was also clearly evidenced in the μ-Raman spectra of $Th_{0.66}Nd_{0.34}O_{1.83}$ and $Th_{0.58}Nd_{0.42}O_{1.79}$. This observation disagreed with the observations made by XRD, since the C-type characteristic XRD lines were only detected for $x_{Nd} \geq 0.45$ (Fig. 4). Such a discrepancy was also described for $Ce_{1-x}Ln_xO_{2-x/2}$ solid solutions [35,99]. It was mainly explained by the sensitivity gap between XRD and μ-Raman. Indeed, XRD could typically be used to distinguish crystallographic ordering over few nanometers range, while μ-Raman is more sensitive and could evidence very local orderings. Consequently, very small C-type domains created because of near-atomic scale local heterogeneities and/or partial segregation of the trivalent lanthanide element toward the grain or the crystallite [101–103] surface over only few nanometer were not evidenced by XRD but easily detectable by μ-Raman. Conversely, the majority of the solid was nonetheless constituted by the F-type phase and the C-type phases detected by μ-Raman for $Th_{0.66}Nd_{0.34}O_{1.83}$ and $Th_{0.58}Nd_{0.42}O_{1.79}$ only represent a minor part of the solid solutions.

For $x_{Nd} \geq 0.45$, the bands related to Nd_2O_3 appeared at 320, 430 and 530 cm^{-1} which fitted well with the spectrum recorded by Denning et al. [104]. Although the A-type phase content was likely low in $Th_{0.55}Nd_{0.45}O_{1.775}$, all the A-type Nd_2O_3 characteristic bands were easily observed, as the confirmation of the high sensitivity of μ-Raman spectroscopy, even in the presence of small quantities of Nd_2O_3 in such mixed-oxides [35].

4. Conclusion

$Th_{1-x}Ln_xO_{2-x/2}$ mixed-oxides, chosen as less radioactive model compounds for future nuclear fuels [46–50,105–107], were produced from homogeneous oxalate precursors. Both precursors and associated mixed-oxides were characterized by IR and μ-Raman spectroscopies, XRD and SEM. From this latter, the final microstructure of resulting oxides was systematically found to be dependent on that of the initial precursor. Moreover, the microstructure of mixed oxalates appeared itself dependent on the crystal structure adopted.

$Th_{0.90}Ln_{0.10}O_{1.95}$, $Th_{0.70}Ln_{0.30}O_{1.85}$ (Ln = Sm, Gd, Dy, Er or Yb) and $Th_{1-x}Nd_xO_{2-x/2}$ mixed-oxides samples were explored mainly through XRD and μ-Raman characterization. Strong similarities were found between $Th_{1-x}Ln_xO_{2-x/2}$ and $Ce_{1-x}Ln_xO_{2-x/2}$ solid

solutions [35]. Indeed, μ-Raman and XRD both confirmed that the substitution of cerium in CeO_2 or thorium in ThO_2 by REE element first occurred through the concomitant formation of oxygen vacancies that allowed the stabilization of the initial fluorite cell and the formation of homogeneous solid solutions. Then, for trivalent cation with ionic radii similar to thorium (mostly for light REE), one can observe the ordering of the oxygen vacancies when increasing the x value ($x \geq 0.4$). This ordering led to the stabilization of C-type $Th_{1-x}Nd_xO_{2-x/2}$ solid solutions.

Furthermore, μ-Raman experiments also evidenced that C-type nano-domains were created for composition with lower substitution rates ($x_{Nd} = 0.34$ and 0.42), as a consequence of local heterogeneities. Likewise, μ-Raman spectroscopy was able to detect very small amount of A-type phase in $Th_{0.51}Nd_{0.49}O_{1.755}$, showing once again the high sensitivity and convenience of this technique to study such mixed-oxides [35–39,99,100]. Moreover, the joined use of XRD and μ-Raman spectroscopy allowed to point out more accurately the limits of stability of the various crystal phases considered. On the basis of XRD results, the variation of the refined unit cell parameters a of $Th_{1-x}Ln_xO_{2-x/2}$ cubic solid solutions versus x followed a polynomial law.

The experimental data collected in this paper were used as an advantage to understand the modifications of $Th_{1-x}Ln_xO_{2-x/2}$ solid solutions properties consequently to the incorporation of trivalent elements. As instance, the chemical durability of such materials (as well as that of $Ce_{1-x}Ln_xO_{2-x/2}$) during leaching tests or dissolution processes were recently found to strongly depend on the lanthanide incorporation rate (and so on the presence of oxygen vacancies) [51,107,108].

Appendix A. Supplementary data

Supplementary data associated with this article can be found, in the online version, at http://dx.doi.org/10.1016/j.materresbull.2012.08.068.

References

[1] I.C. Cosentino, R. Muccillo, Mater. Lett. 32 (1997) 295–300.
[2] R. Ganesan, S. Vivekanandhan, T. Gnanasekaran, G. Periaswami, R.S. Srinivasa, J. Nucl. Mater. 325 (2004) 134–140.
[3] K.H. Kim, D.Y. Kim, K.M. Choi, J.S. Choi, R.G. Sauer, J. Phys. Chem. Solids 50 (1989) 1027–1031.
[4] D.H. Kim, K.M. Choi, K.H. Kim, J.S. Choi, J. Phys. Chem. Solids 50 (1989) 821–828.
[5] Thorium Fuel Cycle – Potential Benefits and Challenges, IAEA Publications, 2005. Available at http://www-pub.iaea.org/MTCD/Publications/PDF/TE_1450_web.pdf, (last checked may 2012).
[6] Y. Tahara, B. Zhu, S. Kosugi, N. Ishikawa, Y. Okamoto, F. Hori, et al. Nucl. Instrum. Methods B 269 (2011) 886–889.
[7] C. Degueldre, J. Bertsch, G. Kuri, M. Martin, Energy Environ. Sci. 4 (2011) 1 651–1661.
[8] M. Lung, O. Gremm, Nucl. Eng. Des. 180 (1998) 133–146.
[9] E. Vapirev, V. Dimitrov, T. Jordanov, I. Christoskov, Nucl. Eng. Des. 167 (1996) 105–112.
[10] C. Lombardi, L. Luzzi, E. Padovani, F. Vettraino, Prog. Nucl. Energ. 50 (2008) 944–953.
[11] E. Merle-Lucotte, L. Matthieu, D. Heuer, V. Ghetta, R. Brissot, C. Le Brun, E. Liatard, Nucl. Technol. 163 (2008) 358–365.
[12] T. Kamei, S. Hakami, Prog. Nucl. Energ. 53 (2011) 820–824.

[13] D. Prieur, A. Jankowiak, T. Delahaye, N. Herlet, P. Dehaudt, P. Blanchart, J. Nucl. Mater. 414 (2011) 503–507.
[14] G.T. Seaborg, Radiochim. Acta 61 (1993) 115–122.
[15] D. Prieur, P.M. Martin, A. Jankowiak, E. Gavilan, A.C. Scheinost, N. Herlet, et al. Inorg. Chem. 50 (2011) 12437–12445.
[16] D. Prieur, F. Lebreton, P.M. Martin, A. Jankowiak, T. Delahaye, P. Dehaudt, et al. J. Eur. Ceram. Soc. 32 (2012) 1585–1591.
[17] D. Prieur, A. Jankowiak, C. Leorier, N. Herlet, L. Donnet, P. Dehaudt, C. Maillard, J.P. Laval, P. Blanchart, Powder Technol. 208 (2011) 553–557.
[18] F. Sibieude, M. Foex, J. Nucl. Mater. 56 (1975) 229–238.
[19] C. Keller, U. Berndt, H. Engerer, L. Leitner, J. Solid State Chem. 4 (1972) 453–465.
[20] M. Aizenshtein, T.Y. Shvareva, A. Navrotsky, J. Am. Ceram. Soc. 93 (2010) 4142–4147.
[21] G. Panneerselvam, M.P. Antony, T. Vasudevan, J. Alloys Compd. 415 (2006) 26–30.
[22] M.D. Mathews, B.R. Ambekar, A.K. Tyagi, J. Alloys Compd. 386 (2005) 234–237.
[23] V. Grover, A.K. Tiagy, J. Am. Ceram. Soc. 89 (2006) 2917–2921.
[24] A.M. Diness, R. Roy, J. Mater. Sci. 4 (1969) 613–624.
[25] C. Adelmann, V. Sriramkumar, V. Van Elshocht, P. Lehnen, T. Conard, S. De Gendt, Appl. Phys. Lett. 91 (2007) 162902–162904.
[26] Y.B. Losovyj, I. Ketsman, A. Sokolov, K.D. Belashchnko, P.A. Dowben, J. Tang, Z. Wang, Appl. Phys. Lett. 91 (2007) 132908–132910.
[27] F. Tcheliebou, M. Boulouz, A. Boyer, Mat. Sci. Eng. B 38 (1996) 90–95.
[28] P. Li, I.-W. Chen, J. Am. Ceram. Soc. 77 (1994) 118–128.
[29] M.O. Zacate, L. Minervini, D.J. Bradfield, R.W. Grimes, K.E. Sickafus, Solid State Ionics 128 (2000) 243–254.
[30] X. Guo, R. Waser, Prog. Mater. Sci. 51 (2006) 151–210.
[31] S.J. Hong, A.V. Virkar, J. Am. Ceram. Soc. 78 (1995) 433–439.
[32] L. Minervini, M.O. Zacate, R.W. Grimes, Solid State Ionics 116 (1999) 339–349.
[33] A. Sachdeva, S.V. Chavan, A. Goswami, A.K. Tyagi, P.K. Pujari, J. Solid State Chem. 178 (2005) 2062–2066.
[34] Y. Ikuma, E. Shimada, N. Okamura, J. Am. Ceram. Soc. 88 (2005) 419–423.
[35] D. Horlait, L. Claparede, N. Clavier, S. Szenknect, N. Dacheux, J. Ravaux, R. Podor, Inorg. Chem. 50 (2011) 7150–7161.
[36] J.R. McBride, K.C. Hass, B.D. Poindexter, W.H. Weber, J. Appl. Phys. 76 (1994) 2435–2442.
[37] W.H. Weber, K.C. Hass, J.R. McBride, Phys. Rev. B 48 (1993) 178–185.
[38] A. Nakajima, A. Yoshihara, M. Ishigame, Phys. Rev. B 50 (1994) 13297–13307.
[39] Z.D. Dohčević-Mitrović, M. Radović, M. Šćepanović, M. Grujić-Brojčin, Z.V. Popović, B. Matović, S. Bošković, Appl. Phys. Lett. 91 (2007) 203118–203123.
[40] L. Li, F. Chen, J.-Q. Lu, M.-F. Luo, J. Phys. Chem. A 115 (2011) 7972–7977.
[41] J. Van Herle, T. Horita, T. Kawada, N. Sakai, H. Yokokawa, M. Doyika, Ceram. Int. 24 (1998) 229–241.
[42] N. Clavier, N. Hingant, M. Rivenet, S. Obbade, N. Dacheux, N. Barré, F. Abraham, Inorg. Chem. 49 (2010) 1921–1931.
[43] B. Arab-Chapelet, S. Grandjean, G. Nowogrocki, F. Abraham, J. Nucl. Mater. 373 (2008) 259–268.
[44] B. Arab-Chapelet, S. Grandjean, G. Nowogrocki, F. Abraham, J. Alloys Compd. 444 (2007) 387–390.
[45] N. Hingant, N. Clavier, N. Dacheux, S. Hubert, N. Barré, R. Podor, L. Aranda, Powder Technol. 208 (2011) 454–460.
[46] N. Hingant, N. Clavier, N. Dacheux, S. Hubert, N. Barré, S. Obbade, F. Taborda, F. Abraham, J. Nucl. Mater. 385 (2009) 400–406.
[47] G. Heisbourg, S. Hubert, N. Dacheux, J. Ritt, J. Nucl. Mater. 321 (2003) 141–151.
[48] S. Hubert, G. Heisbourg, N. Dacheux, P. Moisy, Inorg. Chem. 47 (2008) 2064–2073.
[49] G. Heisbourg, S. Hubert, N. Dacheux, J. Purans, J. Nucl. Mater. 335 (2004) 5–13.
[50] S. Hubert, K. Barthelet, B. Fourest, G. Lagarde, N. Dacheux, N. Baglan, J. Nucl. Mater. 297 (2001) 206–213.
[51] D. Horlait, N. Clavier, S. Szenknect, N. Dacheux, V. Dubois, Inorg. Chem. 51 (2012) 3868–3878.
[52] L. Claparede, N. Clavier, N. Dacheux, A. Mesbah, J. Martinez, S. Szenknect, P. Moisy, Inorg. Chem. 50 (2011) 11702–11714.
[53] L. Claparede, N. Clavier, N. Dacheux, P. Moisy, R. Podor, J. Ravaux, Inorg. Chem. 50 (2011) 9059–9072.
[54] D.-Y. Chung, E.-H. Kim, E.-H. Lee, J.-H. Yoo, J. Ind. Eng. Chem. 4 (1998) 277–284.
[55] K.V. Krishnamurty, G.M. Harris, Chem. Rev. 61 (1960) 213–246.
[56] J. Rodriguez-Carvajal, Physica B 192 (1993) 55–69.
[57] R. Podor, N. Clavier, J. Ravaux, L. Claparede, N. Dacheux, D. Bernache-Assolant, J. Eur. Ceram. Soc. 32 (2012) 353–362.
[58] E. Remy, S. Picart, S. Grandjean, T. Delahaye, N. Herlet, P. Allegri, O. Dugne, R. Podor, N. Clavier, A. Grandjean, P. Blanchart, A. Ayral, J. Eur. Ceram. Soc. 32 (2012) 3199–3209.
[59] R. Podor, J. Ravaux, H.-P. Brau, in: Scanning Electron Microscopy, InTech Publisher, In Situ Experiments in the Scanning Electron Microscope Chamber, 2012, ISBN 978-953-51-0092-82012.
[60] D.E. Morris, D.E. Hobart, J. Raman Spectrosc. 19 (1988) 231–237.
[61] B.A.A. Balboul, Thermochim. Acta 351 (2000) 55–60.
[62] W. Ollendorff, F. Weigel, Inorg. Nucl. Chem. Lett. 5 (1969) 263–269.
[63] J.D. Hanawalt, H.W. Rinn, L.K. Frevel, Anal. Chem. 10 (1938) 457–512.
[64] M.S. Grigor'ev, I.A. Charushnikova, N.N. Krot, Radiochemistry 35 (1997) 419–425.
[65] S. Dash, R. Krishnan, M. Kamruddin, A.K. Tyagi, B. Raj, J. Nucl. Mater. 295 (2001) 281–289.
[66] R. Bressat, B. Claudel, Y. Trambouze, J. Chim. Phys. 60 (1963) 1265.
[67] L. Duvieubourg-Garela, N. Vigier, F. Abraham, S. Grandjean, J. Solid State Chem. 181 (2008) 1899–1908.
[68] D. Louër, F. Deneuve, F. Ecochard, Powder Diffrac. 5 (1990) 104.
[69] A. Ubaldini, C. Artini, G.A. Costa, M.M. Carnasciali, R. Masini, J. Therm. Anal. Calorim. 91 (2008) 797–803.
[70] B.A.A. Balboul, A.Y.Z. Myhoub, J. Anal. Appl. Pyrol. 89 (2010) 95–101.
[71] E. Oktay, A. Yayli, J. Nucl. Mater. 288 (2001) 76–82.
[72] M.T. Aybers, J. Nucl. Mater. 252 (1998) 28–33.
[73] G.D. White, L.A. Bray, P.E. Hart, J. Nucl. Mater. 96 (1981) 305–313.
[74] T. Ohashi, S. Yamazaki, T. Tokunagae, Y. Arita, T. Matsui, T. Harami, K. Kobayashi, Solid State Ionics 113–115 (1998) 559–564.
[75] S. Yamazaki, T. Matsui, T. Ohashi, Y. Arita, Solid State Ionics 136 (2000) 913–920.
[76] H. Hayashi, R. Sagawa, H. Inaba, K. Kawamura, Solid State Ionics 131 (2000) 281–290.
[77] D.R. Ou, T. Mori, F. Ye, J. Zou, G. Auchterlonie, J. Drennan, J. Phys. Rev. B 77 (2008) 024108–24115.
[78] M.R. Levy, C.R. Stanek, A. Chroneos, R.W. Grimes, Solid State Sci. 9 (2007) 588–593.
[79] H. Dachs, Z. Kristall. 107 (1956) 370–395.
[80] V. Grover, A.K. Tyagi, Mater. Res. Bull. 39 (2004) 859–866.
[81] S.V. Chavan, M.D. Mathews, A.K. Tyagi, Mater. Res. Bull. 40 (2005) 1558–1568.
[82] B.P. Mandal, V. Grover, A.K. Tyagi, Mater. Sci. Eng. A 430 (2006) 120–124.
[83] L. Li, G. Li, Y. Che, W. Su, Chem. Mater. 12 (2000) 2567–2574.
[84] T. Hagiwara, Z. Kyo, A. Manabe, H. Yamamura, K. Nomura, J. Ceram. Soc. Jpn. 117 (2009) 1306–1310.
[85] F. Ye, T. Mori, D.R. Ou, J. Zou, J. Drennan, Mater. Res Bull. 43 (2008) 759–764.
[86] V. Grover, A. Banerji, P. Sengupta, A.K. Tyagi, J. Solid State Chem. 181 (2008) 1930–1935.
[87] H. Nitani, T. Nakagawa, M. Yamanouchi, T. Osuki, M. Yuya, T.A. Yamamoto, Mater. Lett. 58 (2004) 2076–2081.
[88] G.G.S. Subramanian, G. Panneerselvam, K.V. Syamala, M.P. Antony, Ceram. Int. 35 (2009) 2185.
[89] S. Hubert, J. Purans, G. Heisbourg, P. Moisy, N. Dacheux, Inorg. Chem. 45 (2006) 3887–3894.
[90] P. Srirama Murti, C.K. Mathews, J. Phys. D: Appl. Phys. 24 (1991) 2202–2209.
[91] R.D. Shannon, Acta. Cryst. A32 (1976) 751–767.
[92] J.S. Bae, W.K. Choo, C.H. Lee, J. Eur. Ceram. Soc. 24 (2004) 1291–1294.
[93] H. Yamamura, S. Takeda, K. Kakinuma, J. Ceram. Soc. Jpn. 115 (2007) 264–269.
[94] L.Z. Vegard, Physica 5 (1921) 17–26.
[95] A.R. Denton, N.W. Ashcroft, Phys. Rev. A 43 (1991) 3161–3164.
[96] L.L. Jensen, J.T. Muckerman, M.D. Newton, J. Phys. Chem. C 112 (2008) 3439–3446.
[97] Y.-F. Li, J.-H. Ouyang, Y. Zhou, X.-S. Liang, J.-Y. Zhong, Bull. Mater. Sci. 32 (2009) 149–153.
[98] K. Nakamoto, Infrared and Raman Spectra of Inorganic and Coordination Compounds, 4th ed., Wiley, New York, 1986.
[99] B.P. Mandal, M. Roy, V. Grover, A.K. Tyagi, Appl. Phys. J. 103 (2008) 033506–33512.
[100] B.P. Mandal, V. Grover, M. Roy, A.K. Tyagi, J. Am. Ceram. Soc. 90 (2007) 61–2965.
[101] Y. Lei, Y. Ito, N.D. Browning, J. Am. Ceram. Soc. 85 (2002) 2359–2363.
[102] V. Bellière, G. Joorst, O. Stephan, F.M.F. de Groot, B.M. Weckhuysen, J. Phys. Chem. B 110 (2006) 9984–9990.
[103] M.-F. Luo, Z.-L. Yan, L.-Y. Jin, M. He, J. Phys. Chem. B 110 (2006) 13068–13073.
[104] J.H. Denning, S.D. Ross, J. Phys. C. Solid State Phys. 5 (1972) 1123–1133.
[105] E. Zimmer, E. Merz, J. Nucl. Mater. 124 (1984) 64–67.
[106] A. Uriarte, R. Rainey, Dissolution of high-density UO_2, PuO_2 and UO_2–PuO_2 pellets in inorganic acids, U.S. Atomic Energy Commision Report ORNL-3695, 1965.
[107] D. Horlait, F. Tocino, N. Clavier, N. Dacheux, S. Szenknect, J. Nucl. Mater. 429 (2012) 237–244.
[108] S. Szenknect, A. Mesbah, D. Horlait, N. Clavier, S. Dourdain, J. Ravaux, N. Dacheux, J. Phys. Chem. C 116 (2012) 12027–12037.